nature physics

Article

https://doi.org/10.1038/s41567-023-02339-2

Universality class of a spinor Bose–Einstein condensate far from equilibrium

Received: 5 April 2023

Accepted: 14 November 2023

Published online: 19 January 2024

Check for updates

SeungJung Huh[1], Koushik Mukherjee[2,3], Kiryang Kwon[1], Jihoon Seo[1], Junhyeok Hur[1], Simeon I. Mistakidis[4,5], H. R. Sadeghpour[4] & Jae-yoon Choi[1]

Scale invariance and self-similarity in physics provide a unified framework for classifying phases of matter and dynamical properties near equilibrium in both classical and quantum systems. This paradigm has been further extended to isolated many-body quantum systems driven far from equilibrium, for which the physical observables exhibit dynamical scaling with universal scaling exponents. Universal dynamics appear in a wide range of scenarios, including cosmology, quark–gluon matter, ultracold atoms and quantum spin magnets. However, how the universal dynamics depend on the symmetry of the underlying Hamiltonian in non-equilibrium systems remains an outstanding challenge. Here we report on the classification of universal coarsening dynamics in a quenched two-dimensional ferromagnetic spinor Bose gas. We observe spatio-temporal scaling of spin correlation functions with distinguishable scaling exponents that characterize binary and diffusive fluids. The universality class of the coarsening dynamics is determined by the symmetry of the order parameter and the dynamics of the topological defects, such as domain walls and vortices. Our results categorize the universality classes of far-from-equilibrium quantum dynamics based on the symmetry properties of the system.

Critical behaviour in thermodynamic equilibrium occurs in both classical and quantum realms. Such static critical phenomena can be divided into universality classes, each class described by the same set of exponents. However, two systems in the same static universality class may belong to different dynamical classes[1]. Extending the concept of universality to far-from-equilibrium quantum many-body systems presents a formidable challenge in physics[2–4]. Numerous experiments with myriad platforms have observed universal behaviour and spatio-temporal scaling of physical observables in late-time dynamics, such that the scaling exponents and scaling functions are independent of the microscopic details and the initial conditions. Celebrated examples are the prethermal dynamics of both a unitary Bose gas[5,6] and the wave turbulence of an atomic superfluid[7], the relaxation dynamics of spin correlations[8] and momentum distributions[9–11], and emergent superdiffusive spin transport[12–14].

Recently, a comprehensive picture of universal dynamics has emerged for isolated quantum systems[15–21] in which quantum states driven far from equilibrium undergo a critical slowing down and display a self-similar time evolution associated with non-thermal fixed points. Universal coarsening dynamics driven by the annihilation of topological defects are found in quenched multicomponent Bose–Einstein condensates[21–25]. This is contrast with the classical theory of phase-ordering kinetics in that the quantum many-body systems are not in contact with a thermal bath[26]. Generalized hydrodynamics has

[1]Department of Physics, Korea Advanced Institute of Science and Technology, Daejeon, South Korea. [2]Department of Mathematical Physics and NanoLund, LTH, Lund University, Lund, Sweden. [3]Department of Physics, Indian Institute of Technology Kharagpur, Kharagpur, India. [4]Institute for Theoretical Atomic Molecular and Optical Physics, Center for Astrophysics, Harvard & Smithsonian, Cambridge, MA, USA. [5]Department of Physics, Harvard University, Cambridge, MA, USA. e-mail: jaeyoon.choi@kaist.ac.kr

been developed for integrable models[27,28]. Moreover, superdiffusive transport in quantum magnets has been predicted[29–31], as described by the Kardar–Parisi–Zhang universality class[32]. However, whether and how the far-from-equilibrium quantum dynamics and their universality classes depend on the symmetries of the Hamiltonian and the emergent topological textures remain unanswered.

Here we address these questions by studying universal coarsening dynamics in a quenched strongly ferromagnetic superfluid in two dimensions. We demonstrate that universality can be classified by: (1) the symmetry of the order parameter in the post-quench phase and (2) the merging and annihilation dynamics of the associated topological defects, such as domain walls and vortices. By quenching the quadratic Zeeman energy (QZE) such that a phase transition is crossed, relatively small magnetic domains are spontaneously generated and subsequently merge to enter the coarsening stage in the long-time evolution. By monitoring the spin correlation functions at various hold times, we confirm that the dynamics are self-similar, regardless of the experimental conditions. Specifically, when the ground state after the quench has $\mathbb{Z}_2$ (spin inversion) symmetry, the domain growth dynamics can be described by the universal scaling exponent $1/z_{\rm exp} \approx 0.58(2)$ $[1/z_{\rm sim} \approx 0.59(1)]$ in the experiment [finite-size simulations]. At high momentum, the so-called Porod tail[26] is also observed in the structure factor as an imprint of the universal character of the dynamics and is associated with the formation of a magnetic domain with sharp edges. Our results show that the emergent dynamics belong to a binary-fluid universality class in the inertial hydrodynamic regime[1,22,24]. When the Hamiltonian exhibits SO(3) spin-rotation symmetry, the characteristics of the ensuing magnetic domain coarsening are modified. In the diffusive growth dynamics of domain length[25], the experimentally (theoretically) measured scaling exponent is $1/z_{\rm exp} \approx 0.43(3)$ $[1/z_{\rm sim} \approx 0.40(1)]$, which belongs to the non-thermal universality class of O(N) symmetric Hamiltonians[21,33]. We identify the formation of spin vortices by matter-wave interferometry and argue that their annihilation is closely related to the observed diffusive dynamics. Note also that the difference in the value of the above exponents with the thermodynamic limit predictions, namely $1/z \approx 2/3$ (refs. 22–24) and $1/z \approx 1/2$ (refs. 21,25,33), respectively, can be attributed to the impact of finite-size effects introduced by the external trap.

Ferromagnetic spin-1 system

Our experiments begin by preparing a two-dimensional (2D) degenerate spin-1 Bose gas of ^{7}Li atoms in an optical dipole trap[34]. The Hamiltonian for the 2D spin-1 condensate is[35,36]

$$H = \int \mathrm{d}^2\mathbf{r}\left[\Psi^\dagger\left(-\frac{\hbar^2\nabla^2}{2M} + qf_z^2 + V_{\rm trap}\right)\Psi + \frac{c_0}{2}n^2 + \frac{c_2}{2}|\mathbf{F}|^2\right], \quad (1)$$

where $\Psi = (\Psi_1, \Psi_0, \Psi_{-1})^{\rm T}$ is the wavefunction of each hyperfine level ($m = -1, 0, 1$), M is the atomic mass, $\mathbf{r} = (x,y)$ and $n = \Psi^\dagger\Psi$ is the atom density in the optical dipole trap $V_{\rm trap}$. The spin density is $\mathbf{F} = (F_x, F_y, F_z)$, where its $j = \{x, y, z\}$ component is $F_j = \Psi_m^\dagger f_j \Psi_m$ with spin-1 matrices f_j. The coefficients c_0 and c_2 represent spin-independent and spin-dependent interaction coefficients, respectively, and q is the QZE. The ^{7}Li spinor gas has ferromagnetic spin interactions ($c_2 < 0$), and its ground state is known to feature different phases[37] depending on the relative strength $q/|c_2|n$ (Fig. 1a). For $q \gg |c_2|n$, the system lies in the polar phase, where it remains unmagnetized and only the $m_z = 0$ component is occupied. The region $0 < q < 2|c_2|n$ is termed the easy-plane phase, having magnetization along the x–y plane and all m_z components being unequally populated. The isotropic point $q = 0$ is where all three spin components are equally populated. Entering $q < 0$, the magnetization resides in the z axis and the phase is known as the easy-axis phase. In the experiment, the degenerate Bose gas is generated under a finite magnetic field to prepare the spinor system in the polar phase (Methods).

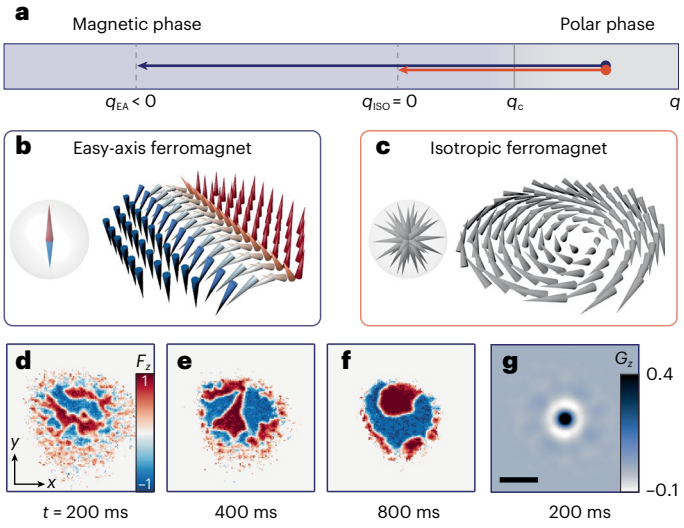

Fig. 1 | Universal coarsening dynamics and topological defects. a, Schematic diagram of the experimental sequence. Ramping the QZE q, the initially prepared polar condensate is quenched to a magnetic phase $q < q_c$. The universal coarsening dynamics are investigated at (1) $q_{\rm EA} < 0$ easy-axis ferromagnetic phases with $\mathbb{Z}_2$ spin symmetry and (2) $q_{\rm Iso} = 0$ isotropic ferromagnetic phase with SO(3) symmetry. **b**,**c**, Cartoon pictures of a magnetic domain in the easy-axis ferromagnetic phase (**b**) and a spin vortex in the isotropic ferromagnetic phase (**c**). The magnetization vectors in each regime are shown as the spin sphere on the left-hand side of the defects. **d**–**f**, Snapshot images of the magnetization at different hold times after quenching the polar condensate to the easy-axis phase, $q_{\rm EA}/h = -200$ Hz: $t = 200$ ms (**d**), $t = 400$ ms (**e**) and $t = 800$ ms (**f**). **g**, Correlation function of longitudinal magnetization $G_z(x, y)$ at $t = 200$ ms. Scale bar, 100 µm. The data are averaged over 100 experimental realizations.

To initiate the non-equilibrium dynamics, we switch on the microwave field to quench the QZE from $q/h = 510$ Hz (polar phase) to a final value (Fig. 1a). This leads to a rapid crossing of the phase boundaries rendering the initial polar state unstable and forming magnetic domains[38]. After a hold time t, we measure the in situ atomic density for each spin state and record the magnetization either along the vertical F_z or the horizontal spin axis F_x (Methods). A key feature of our system is the strongly ferromagnetic spin interactions[34], such that the characteristic time (length) scale is much shorter (smaller) compared to other alkali atomic systems. For instance, the spin interaction energy at the trap centre is $c \approx -h \times 160$ Hz and the characteristic timescale for domain formation is $t_{\rm s} = \hbar/2|c| \approx 0.5$ ms (ref. 38). Such a strong interaction makes it possible to monitor the spinor gas for evolution times $t \approx 2 \times 10^3\, t_{\rm s}$, which is long enough to study the emergent universal coarsening dynamics[22–25]. Domain formation occurs initially at the harmonic trap centre due to the higher spin-dependent interaction energy. Subsequently these small magnetic domains merge and grow in the universal regime with the same power-law exponent regardless of the condensate density. Therefore, we are able to investigate the universal coarsening dynamics even with the density inhomogeneity enforced by the harmonic trap. To validate the experimental observations, we perform extensive simulations of the underlying Gross–Pitaevskii equations tailored to the experimental set-up. The truncated Wigner approximation is employed[39] and accounts for quantum and thermal fluctuations in the initial polar state; see Methods for more details.

Coarsening dynamics with $\mathbb{Z}_2$ symmetry

We first investigate the non-equilibrium dynamics in the easy-axis ferromagnetic phase, $q_{\rm EA}/h = -200$ Hz. The order parameter for the easy axis has $U(1) \times \mathbb{Z}_2$ symmetry, which supports the formation of

https://doi.org/10.1038/s41567-023-02339-2

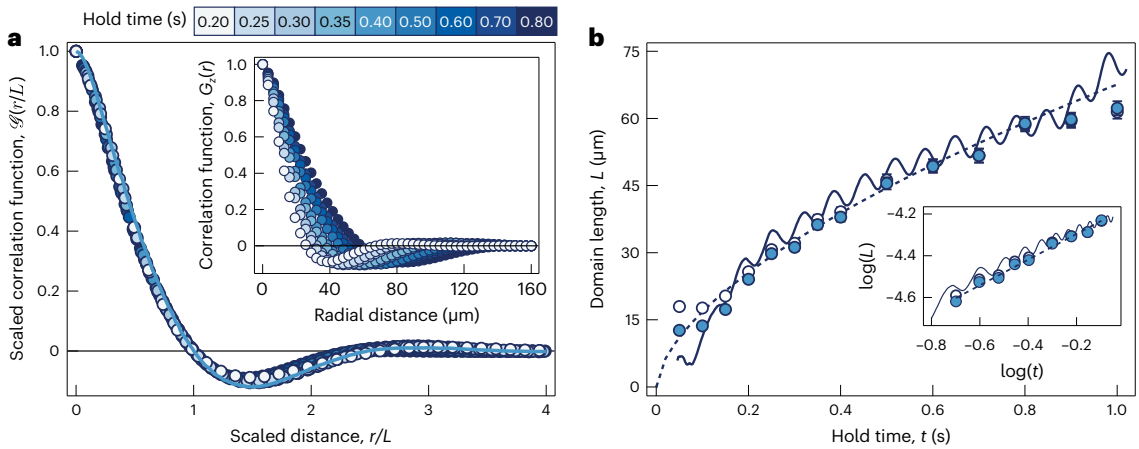

Fig. 2 | Dynamic scaling and power-law growth of the domain length. a, Scaled correlation function $\mathcal{G}(r/L)$ at various hold times, $t \in [0.2\,\text{s}, 0.8\,\text{s}]$. The longitudinal spin correlation functions at various hold times (inset) collapse onto a single function after the radial position is rescaled by a domain length $L(t)$. Here, $L(t)$ is set by a distance with $G_z(r, t) = 0$. The solid light-blue line represents the numerical result with the experimental parameters. **b**, Power-law growth of the domain length $L(t)$. Data with closed (open) circles represent the rescaled domain length after (without) deconvolution. The solid line is the theory line. The oscillatory behaviour comes from the breathing motion of the condensates. The dashed line represents a power-law function $L(t) \approx t^{1/z}$ with $1/z = 0.61$, which is obtained from a linear fit in the log-log plot of the domain growth dynamics (inset). The full dynamics of the domain length are shown in Extended Data Fig. 2, where we carefully choose the scaling range. Small deviations observed at long evolution times between theory and experiment are attributed to atom losses by microwave dressing (Extended Data Fig. 3). Each data point was obtained from more than 100 independent experimental realizations, and one standard error of the mean (s.e.m.) is comparable to the size of the data symbols.

magnetic domain walls as topological defects (Fig. 1b). After the quench, the polar phase is dynamically unstable and atom pairs with $|F = 1, m_z = \pm 1\rangle(|\pm 1\rangle)$ spin states and opposite momenta are generated. The kinetic energy ε_k of the created spin states stems from the post-quench QZE and the associated spin interaction energy $\varepsilon_k = -q_{EA} - c$ (refs. 37,40). Since the kinetic energy is comparable to the condensate chemical potential $\mu/h = 310$ Hz, we can be sure that the spinor gas is driven far from equilibrium. At early times, $t < 10$ ms, spin-mixing takes place and the populations of the spin $|\pm 1\rangle$ states increase exponentially until they reach a steady value after 100 ms (Extended Data Fig. 1). During the spin-mixing process, gauge vortices appear in the $|\pm 1\rangle$ states, which either annihilate or drift out of the condensate, giving their place to magnetic domains (additional data are available in Supplementary Information). Afterwards, the number of spin domains decreases and their size increases, resulting in a process known as coarsening dynamics (Fig. 1d–f). During the coarsening dynamics, the time evolution displays a self-similar behaviour characterized by a universal scaling law such that the condensate is away from both its initial and equilibrium states. For longer evolution times ($t \approx 2$ s), only a few domains are left and coarsening is terminated (Extended Data Fig. 2).

The scaling behaviour can be understood by analysing the equal-time correlation function of the longitudinal magnetization[24], $G_z(\mathbf{r}, t) = \frac{1}{\mathcal{N}} \int \mathrm{d}^2\mathbf{r}' \langle F_z(\mathbf{r} + \mathbf{r}', t) F_z(\mathbf{r}', t)\rangle$, as depicted in Fig. 1g. Here, $\mathcal{N} = \int \mathrm{d}^2\mathbf{r}' \langle F_z(\mathbf{r}', t)^2\rangle$ is the normalization factor, which is conserved during the coarsening stage[8]. In the inset of Fig. 2a, we present the radial profile of the spin correlation functions $G_z(r, t)$ at various hold times. The anti-correlation captured by $G_z(r, t)$ indicates the creation of magnetic domains in opposite spin states. We quantify, both in experiment and theory, the average domain size $L(t)$ as the first zero of the correlation function, $G_z(L, t) = 0$ (ref. 24). Indeed, upon rescaling the radial distance $r \to r/L(t)$, the correlation functions at various hold times collapse onto a single curve, $\mathcal{G}[r/L(t)]$ (Fig. 2a), indicating the self-similar character of the universal dynamics.

The universal growth dynamics are characterized by the power-law increase of the domain length $L(t) \approx t^{1/z}$ (Fig. 2b), where the dynamical critical exponent $1/z$ determines the universality class of the emergent coarsening dynamics. Since in the easy-axis phase the spinor gas reduces to a binary superfluid system consisting of only the $m_z = \pm 1$ components, the coarsening dynamics belong to a binary-fluid universality class or model H (ref. 1). Previous numerical studies operating in the thermodynamic limit indeed confirmed this argument and predicted the scaling exponent to be $1/z = 2/3$ (refs. 22–24).

Figure 2b shows the power-law growth of $L(t)$ as extracted from both experiment and theory. The scaling exponent in the experiment (open circles) is $1/z_{exp} = 0.57(2)$, which is in excellent agreement with our mean-field simulations $1/z_{sim} \approx 0.59(1)$ using the experimental parameters. Here, the time interval for the scaling regime is set to $t \in [0.2\,\text{s}, 0.8\,\text{s}]$, and the independency of the scaling exponent on the time interval is demonstrated (Extended Data Fig. 2a,b). The exponents as found both experimentally and theoretically, however, are smaller than the predicted thermodynamic limit value $1/z = 2/3$ (refs. 22–24), and we attribute this discrepancy to the finite size of our system as enforced by the external trap. Although the universal scaling arguments are strictly valid in the thermodynamic limit, corrections for the finite size should reduce the exponent to $1/z \approx 2/3(1 - \mathcal{O}(\xi_s/L))$ (refs. 23,41), where $\xi_s = \hbar/\sqrt{2M|c|} \approx 2.2$ μm is the spin healing length. This is further supported by our simulations with the harmonic trap, which give a scaling exponent $1/z_{sim} = 2/3$ at large atom number ($N \approx 10^8$) (see Supplementary Information). Furthermore, our imaging system has an effective resolution of 5 μm, which could increase the domain length. Employing the Weiner deconvolution method, we recalibrate the domain size and obtain $1/z_{exp} = 0.61(3)$. Similar universal behaviour is observed in counting the magnetic domain number after the quench (Extended Data Fig. 2c).

Dynamical scaling is also represented in the structure factor $S_z(k, t) = L(t)^2 S_u(kL(t))$, which is the Fourier transformation of the spin correlation function, with a scaling function S_u (ref. 24). The scaling form is identical to the non-thermal fixed point theory, which suggests that $S_z(k, t) = t^{d/z} f_S(t^{1/z}k)$ in d spatial dimensions with f_S a scaling function[16–21]. Figure 3 shows the rescaled structure factors within the time interval $t \in [0.2\,\text{s}, 0.8\,\text{s}]$. A universal scaling of the Porod tail $S_z(k) \approx k^{-3}$ is observed[26]. At early times ($t < 100$ ms), we observe that the structure factor monotonically decreases (not shown), and only after the system enters the coarsening stage, are the characteristic 'knee' shape and the universal high-momentum tail, revealed. The k^{-3} scaling behaviour originates from a linear decay of the correlation function with sharp

https://doi.org/10.1038/s41567-023-02339-2

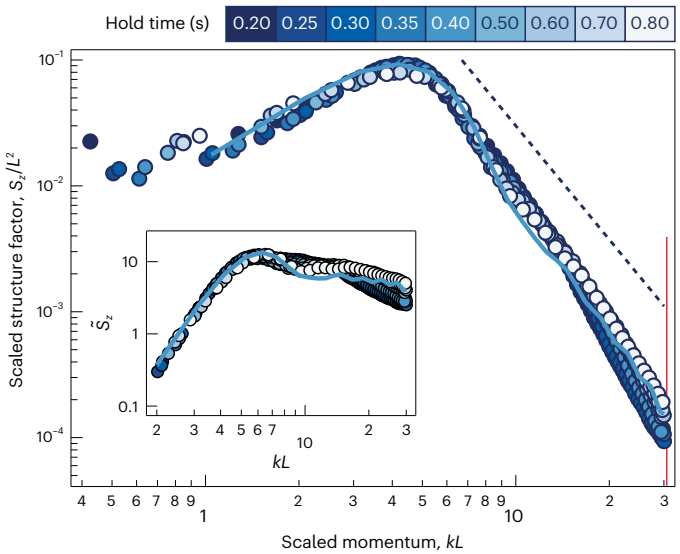

Fig. 3 | Dynamic scaling of the spin structure factor in the easy-axis quench. The structure factor of longitudinal magnetization $S_z(k, t)$ is rescaled by the domain length: $S_z \to S_z/L^2$ and $k \to kL$. The dashed line is the universal Porod tail $S_z(k, t) \approx k^{-3}$ with an offset for clarity. The vertical red line represents the momentum resolution for $t = 0.2$ s. As time progresses, the high-momentum tail tends towards the universal k^{-3} scaling. Deviations from k^{-3} scaling at higher momenta are traced back to the finite imaging resolution of the CCD pixel (3.2 µm) in the experiment and the finite spatial discretization in the simulations. The inset shows the structure factor with compensation, $\tilde{S}_z = S_z(k, t)Lk^3$. The solid light-blue line is the numerically calculated structure factor upon rescaling at $t \approx 0.8$ s.

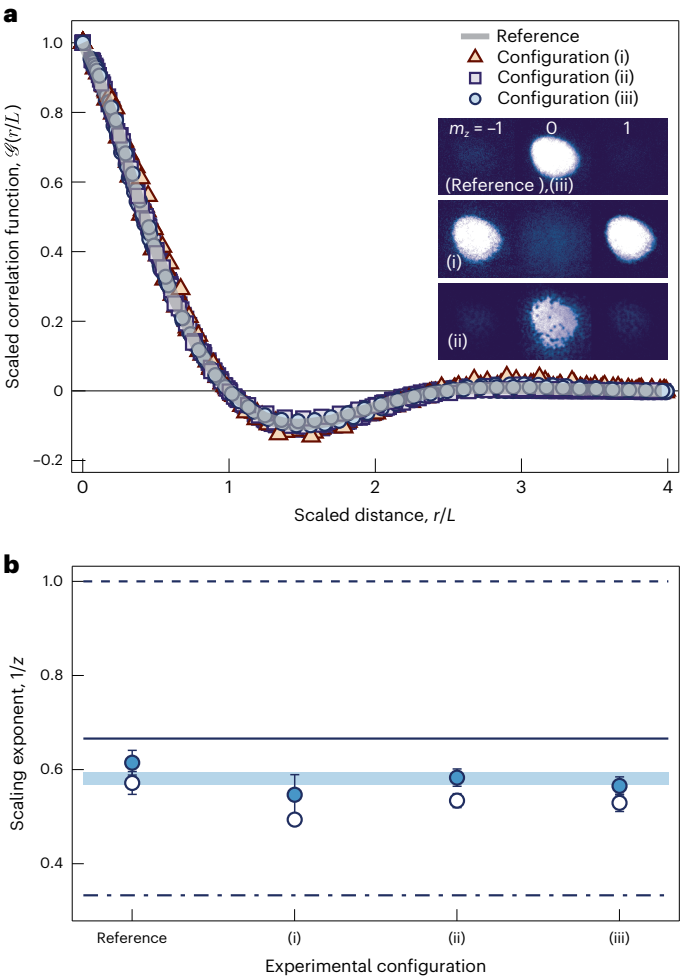

Fig. 4 | Universal coarsening dynamics in the easy-axis phase. a, Scaled spin correlation functions $\mathcal{G}(r/L)$ in the coarsening stage for four different experimental configurations (see main text). The reference experiment refers to the coarsening dynamics at $q_{EA}/h = -200$ Hz with a polar-phase initial state (Fig. 2a). The inset shows spin-resolved absorption images for various initial conditions. The vortices in (ii) can be identified after 6 ms of time of flight. **b**, Dynamical scaling exponents for the different configurations (Fig. 4a). Data with closed (open) circles represent the exponent after (without) deconvolution. Error bars denote the fitting errors (the resampling error is smaller than the fitting errors). The shaded line shows the results of numerical calculations with a finite system size. The solid line indicates the dynamic exponents for the inertial hydrodynamic regime in the thermodynamic limit, $1/z = 2/3$. The experimental results are distinguished from other dynamic exponents in a binary-fluid universality class in the viscous $1/z = 1$ (dashed line) and diffusive $1/z = 1/3$ (dashed-dotted line) regimes.

domain wall edges among the $m_z = \pm 1$ states[26], which is confirmed in our experiment by imaging F_z and F_x (Extended Data Fig. 4).

To demonstrate universality, we further investigate the quench dynamics with three different experimental configurations: (i) We create an equal superposition of $|\pm 1\rangle$ states at $q/h = 510$ Hz as the initial state and study the quench dynamics at $q_{EA}/h = -200$ Hz. The initial state has a different dynamical response from the polar condensate[37,42], and we observe domain separation[43] instead of spin pair generation. (ii) Many vortices and anti-vortices are imprinted in the polar condensate by dragging a repulsive barrier before the quench (Methods), and we investigate the effect of vortices on the coarsening dynamics. (iii) We prepare the polar condensate and quench QZE to $q_{EA}/h = -120$ Hz, which is smaller than the reference experiment ($q_{EA}/h = -200$ Hz) but still in the easy-axis phase. In this case, the decay time of $L(t)$ from the microwave dressing is increased from 7 to 40 s. Even with such diverse experimental configurations, we obtain the same universal curve upon rescaling the spin correlation function (Fig. 4a), and the dynamical scaling exponents are all approximately $1/z_{exp} \approx 0.58(2)$ (Fig. 4b). This highlights the insensitivity of the universal coarsening dynamics to experimental details, which contrasts with the near equilibrium critical phenomena[1] that require a fine-tuning of system parameters. Here, we find similar results when the universal scaling functions are obtained by satisfying the scaling form $G_z(r, t) = f_G(t^{-\beta}r)$ and $S_z(k, t) = t^{\alpha}f_S(t^{\beta}k)$ with universal scaling exponents α and β (materials are available in Supplementary Information). Furthermore, the scaling exponent is far different from that of other universality classes of binary fluids, such as viscous hydrodynamics with $1/z = 1$ or diffusive dynamics with $1/z = 1/3$ (ref. 26). We reaffirm that the coarsening dynamics of the 2D ferromagnetic superfluid in the easy-axis phase belongs to the binary-fluid universality class in the inertial hydrodynamic regime[1].

Coarsening dynamics with SO(3) symmetry

We now turn our attention to examining the coarsening dynamics at $q_{Iso} = 0$ (Fig. 1c). In contrast to the easy-axis phase, the ground state is invariant under spin rotations. Therefore, we aim to investigate the impact of the symmetry of the order parameter, here obeying SO(3) rotational symmetry, and the nature of topological defects on the universal behaviour of the spinor system. As the first homotopy group of SO(3) is $\pi_1[\mathrm{SO}(3)] = \mathbb{Z}_2$, the condensate supports $\mathbb{Z}_2$ spin vortices as topological defects[37]. A recent study argued that universal coarsening dynamics also occur at the spin isotropic point, as in the easy-axis phase, but with a different critical exponent $1/z = 0.5$ (ref. 25). This result is consistent with the theory of non-thermal fixed points, which predicts the dynamical scaling exponent $1/z \approx 0.5$ for a bosonic Hamiltonian with O(N) or U(N) symmetry in $d \geq 2$ dimensions[21,33]. Additionally, a numerical study within the mean-field framework[25] also reported that the coarsening dynamics proceeds with the annihilation of $\mathbb{Z}_2$ spin vortices.

Figure 5 summarizes our experimental results for the coarsening dynamics with a spin isotropic Hamiltonian. Since the spin vectors can

https://doi.org/10.1038/s41567-023-02339-2

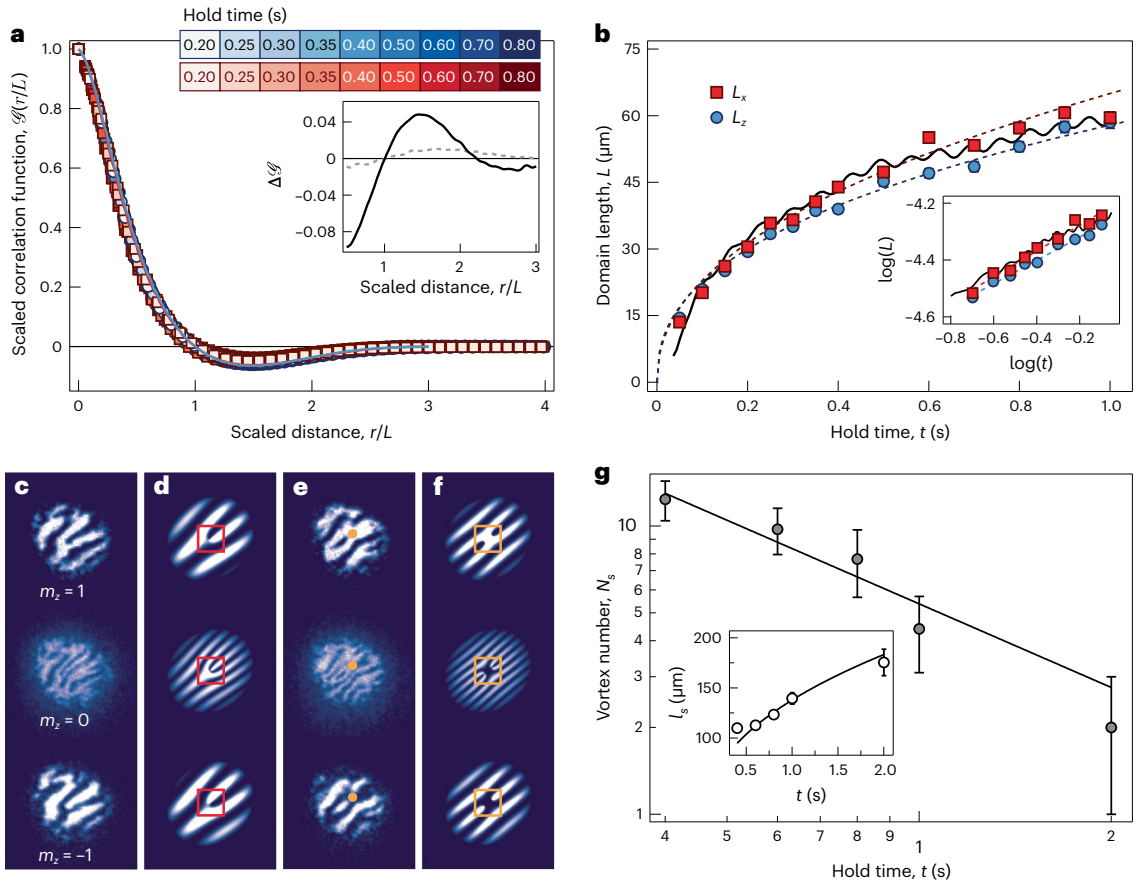

Fig. 5 | Coarsening dynamics in the isotropic ferromagnetic phase. a, Scaled correlation functions of the magnetization along the x axis (red squares) and z axis (blue circles) from the experiment and theory (solid lines). The domain length $L(t)$ is characterized by the first zero of the correlation function for both axes, $G_{x,z}(L, t) = 0$. Inset: differences in the scaled correlation functions. The solid line is $\Delta\mathcal{G} = \mathcal{G}_{q_{\rm Iso}} - \mathcal{G}_{q_{\rm EA}}$, where $\mathcal{G}_{q_{\rm Iso}} = (\mathcal{G}_x + \mathcal{G}_z)/2$ and $\mathcal{G}_{q_{\rm EA}}$ are obtained from interpolating data in Fig. 2a. The dashed line is $\mathcal{G}_x - \mathcal{G}_z$. **b**, Growth dynamics of the spin domain for each axis. The solid line is the numerical result using our experimental parameters. The inset shows a log-log plot of the domain length dynamics. We extracted the scaling exponent with linear fits (dashed lines). **c**, Matter-wave interference images during the coarsening dynamics ($t = 1$ s). The two-to-one (three-to-one) fork-shaped fringes in the spin $|\pm1\rangle$ ($|0\rangle$) state represent phase windings of 2π (4π) around the vortex core. **d**, Simulated interference pattern with a spin vortex at the trap centre (red boxes). **e**, Interference images with spin vortex and anti-vortex pairs at $t = 1$ s (orange circles). **f**, Numerical simulations with the vortex pair located at the trap centre (H-shaped pattern, orange boxes). **g**, Number of spin vortices N_S as a function of time. Inset: the intervortex distance l_S during the time evolution. Solid lines are power-law guidelines, $N_S(t) \approx 1/L(t)^2$ and $l_S \approx L(t)$. The vortex number is the average over 40 independent realizations, and the error bars indicate 1 s.e.m.

point in an arbitrary direction, domain coarsening is observed for both F_x and F_z (Extended Data Fig. 5). Following the same analysis as in the easy-axis quench experiment, we rescale the correlation functions by $L(t)$ and observe their collapse into a single curve (Fig. 5a), in line with the mean-field analysis. These universal curves are similar for each spin axis measured but are distinctive from those of the easy-axis quench experiment (Fig. 5a inset), implying that the dynamics at the spin isotropic point belong to a different universality class. This can be further supported by the scaling exponent of the domain length $L(t) \approx t^{1/z}$ (Fig. 5b), which we experimentally find to be $1/z_{\rm exp} \approx 0.45(3)$ for F_x and $1/z_{\rm exp} \approx 0.41(2)$ for F_z. Here, the exponents are close to the thermodynamic prediction $1/z = 0.5$ (ref. 25) and show good agreement with our finite-size numerical simulations, $1/z_{\rm sim} \approx 0.40(1)$.

To identify the underlying mechanism responsible for the coarsening dynamics in the SO(3) phase, we monitor the spin vortices and study their decay dynamics during the coarsening stage. Matter-wave interferometry was adopted to identify the position of the vortex cores from the relative phase winding between spin states (Methods). Characteristic interference patterns of the spin vortices are shown in Fig. 5c. The fork-shaped fringes are well represented in all three spin components. We also observe events with closely bounded spin vortex/anti-vortex pairs (Fig. 5e). The existence of these spin vortices and vortex pairs is well reproduced in the simulated interference images (Fig. 5d,f and Extended Data Fig. 6).

By assigning the position of the spin vortex (vortex pairs) to the joint point in the fork-shaped (H-shaped) patterns, we count the spin vortex number N_S and calculate the average distance between vortices l_S at various hold times (Fig. 5g). The vortex number gradually decays, whereas the mean distance increases as time evolves. Since the imaging resolution is larger than the spin healing length, we underestimate the vortex number when the condensate contains many vortices. Nevertheless, the vortex number scales with the domain size, such that $N_S \approx 1/L(t)^2$ and $l_S \approx L(t)$. The decay of spin vortex pairs occurs at a similar timescale (materials are available in Supplementary Information), hinting at its intricate connection with the universal coarsening dynamics in the isotropic SO(3) symmetric phase. This is supported by our numerical simulations, as we calculated the argument of the transverse spin vector and tracked the respective phase jumps (materials are available in Supplementary Information).

Conclusions and outlook

Utilizing a strongly ferromagnetic spinor condensate, we observe universal coarsening dynamics in two dimensions. We find that the universal dynamics can be categorized into a well-defined universality

class based on the symmetry of the order parameter and the dynamics of topological defects, such as domain walls and spin vortices. Our research demonstrates the diverse capabilities of cold-atom quantum simulators in characterizing non-equilibrium quantum dynamics, thus providing a stepping stone to a comprehensive understanding of quantum thermalization processes in multidisciplinary research fields. Further extensions include an investigation of the universal dynamics mediated by other types of excitations, such as vortices in a two-dimensional superfluid[44–46], solitons in one dimension[47,48], magnons in the Heisenberg spin model[49,50] and chiral quantum magnetization with spin–orbit interactions[51,52]. Moreover, our strongly interacting platform offers new opportunities for exploring long-time thermalization dynamics in two dimensions, as the long-lived topological defects can slow down equilibration[53].

Online content

Any methods, additional references, Nature Portfolio reporting summaries, source data, extended data, supplementary information, acknowledgements, peer review information; details of author contributions and competing interests; and statements of data and code availability are available at https://doi.org/10.1038/s41567-023-02339-2.

References

1. Hohenberg, P. C. & Halperin, B. I. Theory of dynamic critical phenomena. *Rev. Mod. Phys.* **49**, 435–479 (1977).
2. Polkovnikov, A., Sengupta, K., Silva, A. & Vengalattore, M. Colloquium: nonequilibrium dynamics of closed interacting quantum systems. *Rev. Mod. Phys.* **83**, 863–883 (2011).
3. Eisert, J., Friesdorf, M. & Gogolin, C. Quantum many-body systems out of equilibrium. *Nat. Phys.* **11**, 123–130 (2015).
4. Ueda, M. Quantum equilibration, thermalization and prethermalization in ultracold atoms. *Nat. Rev. Phys.* **2**, 669–681 (2020).
5. Makotyn, P., Klauss, C. E., Goldberger, D. L., Cornell, E. A. & Jin, D. S. Universal dynamics of a degenerate unitary Bose gas. *Nat. Phys.* **10**, 116–119 (2014).
6. Eigen, C. et al. Universal prethermal dynamics of Bose gases quenched to unitarity. *Nature* **563**, 221–224 (2018).
7. Gałka, M. et al. Emergence of isotropy and dynamic scaling in 2D wave turbulence in a homogeneous Bose gas. *Phys. Rev. Lett.* **129**, 190402 (2022).
8. Prüfer, M. et al. Observation of universal dynamics in a spinor Bose gas far from equilibrium. *Nature* **563**, 217–220 (2018).
9. Erne, S., Bücker, R., Gasenzer, T., Berges, J. & Schmiedmayer, J. Universal dynamics in an isolated one-dimensional Bose gas far from equilibrium. *Nature* **563**, 225–229 (2018).
10. Glidden, J. A. P. et al. Bidirectional dynamic scaling in an isolated Bose gas far from equilibrium. *Nat. Phys.* **17**, 457–461 (2021).
11. Fontaine, Q. et al. Kardar–Parisi–Zhang universality in a one-dimensional polariton condensate. *Nature* **608**, 687–691 (2022).
12. Zu, C. et al. Emergent hydrodynamics in a strongly interacting dipolar spin ensemble. *Nature* **597**, 45–50 (2021).
13. Wei, D. et al. Quantum gas microscopy of Kardar–Parisi–Zhang superdiffusion. *Science* **376**, 716–720 (2022).
14. Joshi, M. K. et al. Observing emergent hydrodynamics in a long-range quantum magnet. *Science* **376**, 720–724 (2022).
15. Baier, R., Mueller, A. H., Schiff, D. & Son, D. T. 'Bottom-up' thermalization in heavy ion collisions. *Phys. Lett. B* **502**, 51–58 (2001).
16. Berges, J., Rothkopf, A. & Schmidt, J. Nonthermal fixed points: effective weak coupling for strongly correlated systems far from equilibrium. *Phys. Rev. Lett.* **101**, 041603 (2008).
17. Schole, J., Nowak, B. & Gasenzer, T. Critical dynamics of a two-dimensional superfluid near a nonthermal fixed point. *Phys. Rev. A* **86**, 013624 (2012).
18. Schmidt, M., Erne, S., Nowak, B., Sexty, D. & Gasenzer, T. Non-thermal fixed points and solitons in a one-dimensional Bose gas. *New J. Phys.* **14**, 075005 (2012).
19. Berges, J., Boguslavski, K., Schlichting, S. & Venugopalan, R. Turbulent thermalization process in heavy-ion collisions at ultrarelativistic energies. *Phys. Rev. D* **89**, 074011 (2014).
20. Berges, J., Boguslavski, K., Schlichting, S. & Venugopalan, R. Universality far from equilibrium: from superfluid Bose gases to heavy-ion collisions. *Phys. Rev. Lett.* **114**, 061601 (2015).
21. Piñeiro Orioli, A., Boguslavski, K. & Berges, J. Universal self-similar dynamics of relativistic and nonrelativistic field theories near nonthermal fixed points. *Phys. Rev. D* **92**, 025041 (2015).
22. Kudo, K. & Kawaguchi, Y. Magnetic domain growth in a ferromagnetic Bose–Einstein condensate: effects of current. *Phys. Rev. A* **88**, 013630 (2013).
23. Hofmann, J., Natu, S. S. & Das Sarma, S. Coarsening dynamics of binary Bose condensates. *Phys. Rev. Lett.* **113**, 095702 (2014).
24. Williamson, L. A. & Blakie, P. B. Universal coarsening dynamics of a quenched ferromagnetic spin-1 condensate. *Phys. Rev. Lett.* **116**, 025301 (2016).
25. Williamson, L. A. & Blakie, P. B. Coarsening dynamics of an isotropic ferromagnetic superfluid. *Phys. Rev. Lett.* **119**, 255301 (2017).
26. Bray, A. J. Theory of phase-ordering kinetics. *Adv. Phys.* **43**, 357–459 (1994).
27. Bertini, B., Collura, M., De Nardis, J. & Fagotti, M. Transport in out-of-equilibrium *XXZ* chains: exact profiles of charges and currents. *Phys. Rev. Lett.* **117**, 207201 (2016).
28. Castro-Alvaredo, O. A., Doyon, B. & Yoshimura, T. Emergent hydrodynamics in integrable quantum systems out of equilibrium. *Phys. Rev. X* **6**, 041065 (2016).
29. Ljubotina, M., Žnidarič, M. & Prosen, T. Spin diffusion from an inhomogeneous quench in an integrable system. *Nat. Commun.* **8**, 16117 (2017).
30. Gopalakrishnan, S. & Vasseur, R. Kinetic theory of spin diffusion and superdiffusion in *XXZ* spin chains. *Phys. Rev. Lett.* **122**, 127202 (2019).
31. Ljubotina, M., Žnidarič, M. & Prosen, T. Kardar–Parisi–Zhang physics in the quantum Heisenberg magnet. *Phys. Rev. Lett.* **122**, 210602 (2019).
32. Kardar, M., Parisi, G. & Zhang, Y.-C. Dynamic scaling of growing interfaces. *Phys. Rev. Lett.* **56**, 889–892 (1986).
33. Mikheev, A. N., Schmied, C.-M. & Gasenzer, T. Low-energy effective theory of nonthermal fixed points in a multicomponent Bose gas. *Phys. Rev. A* **99**, 063622 (2019).
34. Huh, S., Kim, K., Kwon, K. & Choi, J.-y. Observation of a strongly ferromagnetic spinor Bose–Einstein condensate. *Phys. Rev. Res.* **2**, 033471 (2020).
35. Ho, T.-L. Spinor Bose condensates in optical traps. *Phys. Rev. Lett.* **81**, 742–745 (1998).
36. Ohmi, T. & Machida, K. Bose–Einstein condensation with internal degrees of freedom in alkali atom gases. *J. Phys. Soc. Jpn* **67**, 1822–1825 (1998).
37. Kawaguchi, Y. & Ueda, M. Spinor Bose–Einstein condensates. *Phys. Rep.* **520**, 253–381 (2012).
38. Sadler, L. E., Higbie, J. M., Leslie, S. R., Vengalattore, M. & Stamper-Kurn, D. M. Spontaneous symmetry breaking in a quenched ferromagnetic spinor Bose–Einstein condensate. *Nature* **443**, 312–315 (2006).
39. Blakie, P. B., Bradley, A. S., Davis, M. J., Ballagh, R. J. & Gardiner, C. W. Dynamics and statistical mechanics of ultra-cold Bose gases using c-field techniques. *Adv. Phys.* **57**, 363–455 (2008).
40. Kim, K., Hur, J., Huh, S., Choi, S. & Choi, J.-y. Emission of spin-correlated matter-wave jets from spinor Bose–Einstein condensates. *Phys. Rev. Lett.* **127**, 043401 (2021).

41. Huse, D. A. Corrections to late-stage behavior in spinodal decomposition: Lifshitz–Slyozov scaling and Monte Carlo simulations. *Phys. Rev. B* **34**, 7845–7850 (1986).
42. Bourges, A. & Blakie, P. B. Different growth rates for spin and superfluid order in a quenched spinor condensate. *Phys. Rev. A* **95**, 023616 (2017).
43. De, S. et al. Quenched binary Bose–Einstein condensates: spin-domain formation and coarsening. *Phys. Rev. A* **89**, 033631 (2014).
44. Gauthier, G. et al. Giant vortex clusters in a two-dimensional quantum fluid. *Science* **364**, 1264–1267 (2019).
45. Johnstone, S. P. et al. Evolution of large-scale flow from turbulence in a two-dimensional superfluid. *Science* **364**, 1267–1271 (2019).
46. Karl, M. & Gasenzer, T. Strongly anomalous non-thermal fixed point in a quenched two-dimensional Bose gas. *New J. Phys.* **19**, 093014 (2017).
47. Schmied, C.-M., Prüfer, M., Oberthaler, M. K. & Gasenzer, T. Bidirectional universal dynamics in a spinor Bose gas close to a nonthermal fixed point. *Phys. Rev. A* **99**, 033611 (2019).
48. Fujimoto, K., Hamazaki, R. & Ueda, M. Flemish strings of magnetic solitons and a nonthermal fixed point in a one-dimensional antiferromagnetic spin-1 Bose gas. *Phys. Rev. Lett.* **122**, 173001 (2019).
49. Bhattacharyya, S., Rodriguez-Nieva, J. F. & Demler, E. Universal prethermal dynamics in Heisenberg ferromagnets. *Phys. Rev. Lett.* **125**, 230601 (2020).
50. Rodriguez-Nieva, J. F., Orioli, A. P. & Marino, J. Far-from-equilibrium universality in the two-dimensional Heisenberg model. *Proc. Natl Acad. Sci. USA* **119**, 2122599119 (2022).
51. Dzyaloshinsky, I. A thermodynamic theory of 'weak' ferromagnetism of antiferromagnetics. *J. Phys. Chem. Solids* **4**, 241–255 (1958).
52. Moriya, T. Anisotropic superexchange interaction and weak ferromagnetism. *Phys. Rev.* **120**, 91–98 (1960).
53. Guzman, J. et al. Long-time-scale dynamics of spin textures in a degenerate $F=1$ ^{87}Rb spinor Bose gas. *Phys. Rev. A* **84**, 063625 (2011).

Methods

Experimental systems

We created a spinor condensate of ^{7}Li atoms in a quasi-2D optical dipole trap[34], with frequencies $(\omega_x, \omega_y, \omega_z) = 2\pi \times (7, 8, 635)$ Hz. The condensate contained 2.7×10^6 atoms and had a negligible thermal fraction (<5%). The chemical potential of the condensate was $\mu/h = 310$ Hz, indicating that transversal excitations were suppressed. Indeed, no spin structures were observed along the axial direction, and thus, we confirmed that the coarsening dynamics occurred in two dimensions. To prepare the condensate in the polar phase, an external magnetic field of $B = 1$ G was applied along the vertical axis. Under this magnetic field, the QZE was larger than the critical point $q > q_c = 2|c|$ (Fig. 1a), so that all atoms populated the same spin state $|F = 1, m_z = 0\rangle \equiv |1, 0\rangle$.

Instantaneous quenching of the QZE was experimentally realized with the microwave dressing technique[40]. The QZE is given by $q = q_B + q_{MW}$, where $q_B/h = \alpha B^2$ is the second-order Zeeman splitting of the hyperfine states of ^{7}Li atoms with $\alpha = 610$ Hz G^{-2}, and $q_{MW}/h = \Omega^2/4\delta$ denotes the respective energy shift due to the microwave field. In the experiment, we ramped the external bias field down to $B \approx 100$ mG in 7 ms and simultaneously tuned the microwave frequency, such that the QZE was always larger than the critical point ($q > q_c$) during the field ramp. We initiated the non-equilibrium dynamics of the spinor gas by changing the microwave frequency within 1 µs and quenching the QZE to a target point. The magnitude of the QZE was calibrated by studying statistics of the spin population at 2 s after the quench[53]. The field gradient was compensated to below 30 µG cm^{-1} so that we observed randomly oriented domain walls, even a long time after the quench ($t = 2$ s). The microwave field induced atom loss and heating during the hold time, as it couples the atoms to the $F = 2$ spin state (Extended Data Fig. 3). Atom loss was noticeable in the deep easy-axis regime ($q/h = -200$ Hz), and we could easily underestimate the domain length and the dynamic scaling exponent. Fortunately, the atom loss was noticeable only for very long times, when all domains had merged, so that the thermal fraction remained mainly below 10% throughout the evolution. Therefore, neither the atom loss nor the heating had any sizeable effect on the universal coarsening dynamics.

Long-term drifts in the experimental parameters were calibrated by taking reference images. For example, the average magnetization at $t = 2$ s was monitored every 150 min (corresponding to approximately 300 measurements), and we adjusted the field gradient if needed. The uncertainty of the QZE was mostly due to the external field noise, which was ±0.3 Hz. The small fluctuations in the QZE were negligible, even for the spin isotropic coarsening dynamics within the considered timescales. The small but non-zero QZE could have led to a coarsening transition at longer evolution times when the scaling exponents of the domain lengths followed the easy-plane or easy-axis phase dynamics[25]. The field fluctuations in the experiment were $q/q_0 < 10^{-3}$ so that the transition occurred after $t > 1$ s ($t > 2{,}000t_s$).

In situ spin-resolved imaging

Atomic density distributions in the lower hyperfine spin states were recorded using the standard absorption imaging technique after selectively converting a target spin state into an upper hyperfine state. Under a magnetic field of 100 mG, for instance, we applied a microwave that transferred the atoms from the $|1, 1\rangle$ to the $|2, 1\rangle$ state. The atomic distribution in the $|2, 1\rangle$ state was subsequently imaged by a resonant light with the $|F = 2\rangle \rightarrow |F' = 3\rangle$ transition. The atoms in the other spin states were measured in a similar manner. Namely, after taking the first image, we applied an additional microwave pulse, flipping the hyperfine spin states from $|1, 0\rangle$ ($|1, -1\rangle$) to $|2, 1\rangle$ ($|2, -2\rangle$), and imaging the transferred atoms. To avoid cross-talk between images within the $F = 1$ state, we removed all atoms in the $|F = 2\rangle$ state before taking subsequent images. This imaging sequence was also used to measure the magnetization along the spin x direction, F_x. Indeed, by applying a resonant radio-frequency pulse, we rotated the measurement basis from the spin z axis to the x axis and recorded the density distribution of each spin state. Paradigmatic images of magnetization along x and z following a quench to the spin isotropic point ($q_{Iso} = 0$) are shown in Extended Data Fig. 5.

To characterize the imaging resolution, we prepared a spin spiral structure, which displayed periodic density modulation in each spin state. This state can be created by evolving the spin vector in the horizontal plane under a finite field gradient[54]. The modulation period λ_{sp} was determined by the gradient strength and exposure time, and the contrast was affected by our imaging system. For example, the contrast dropped to 30% at $\lambda_{sp} = 10$ µm. By investigating the dependence of the contrast on the wavelength λ_{sp}, we estimated that the imaging resolution was 5 µm. The imaging parameters were optimized to give a better signal-to-noise ratio and imaging resolution. We set the imaging light intensity to $0.5I_{sat}$ and the imaging pulse to 4 µs, where $I_{sat} = 2.5$ mW cm^{-2} is the saturation intensity.

Vortex shedding in the polar condensate

To demonstrate the insensitivity of the dynamical exponent on the initial conditions, we imprinted many vortices in the polar phase before the quench. An initial state containing many vortices can be prepared by adopting the vortex-shedding technique[55,56]. Specifically, a repulsive optical barrier was imposed at the trap centre and translated by a piezo mirror mount. When the speed of the barrier exceeded a critical threshold, vortices and anti-vortices were nucleated in the condensate[55]. The optical obstacle was made of focused, blue-detuned laser light of 532 nm along the z direction. Its $1/e^2$ beam waist was 8 µm, and the obstacle height was $V_0/\mu \approx 3$. The sweeping distance of the barrier from the trap centre was $d = 60$ µm, and its translation speed was 6 mm s^{-1}. The vortex cores could be identified after 6 ms of time of flight (inset of Fig. 4a). Around 15 vortices were nucleated before the quench. Indeed, using this initial state containing vortices we performed the quench dynamics as described above and measured the critical exponent, which remained unaffected, for example having the value $1/z = 0.58(2)$ for the easy-axis phase.

Matter-wave interference

To infer the spin windings of spin vortices, we employed matter-wave interference[57,58] with the following experimental procedure. A field gradient of 60 mG cm^{-1} was applied to the condensate for $t_{grad} = 6$ ms. Next, a resonant radio-frequency pulse was used to induce the $|1, 0\rangle \leftrightarrow |1, \pm 1\rangle$ transition. Finally, we imaged all spin components in the $F = 1$ state using the selective spin transfer imaging technique. In the vortex-free state, we observed stripe lines along the gradient direction as a result of the phase accumulation across the condensate. With the phase defect, however, the stripe lines were dislocated, and we could read out the magnitude of the relative phase winding in the spin texture. Because of our finite imaging resolution, we set the periodicity of the stripe patterns to ~10 µm. Accordingly, this became the minimum distance between spin vortices detected with this scheme. The vortex positions in the numerical simulations, as determined by analysing the spin vector, were the same as the phase singular points that were identified using the matter-wave interference technique (Extended Data Fig. 6).

Mean-field equations of the spin-1 gas

The dynamics of the spin-1 condensate is described by the following set of coupled three-dimensional (3D) Gross–Pitaevskii equations of motion:

$$\frac{\partial \Psi(\mathbf{r}; t)}{\partial t} = \left[-\frac{\hbar^2 \nabla^2}{2M} + V_{trap}(\mathbf{r}) + q f_z^2 + c_0 n(\mathbf{r}; t) + c_2 \mathbf{F}(\mathbf{r}; t) \cdot \mathbf{f} \right] \Psi(\mathbf{r}; t). \quad (2)$$

The wavefunction of each hyperfine $m_z = -1, 0$ or 1 level is denoted by $\Psi = (\Psi_1, \Psi_0, \Psi_{-1})^T$, the atom mass is M and $\mathbf{r} \equiv \{x, y, z\}$. The spin-independent nonlinear term $c_0 n$ is characterized by the effective strength, $c_0 = 4\pi\hbar^2(a_0 + a_2)/(3M)$, and total density, $n = \sum_{m_z} |\Psi_{m_z}|^2$. Here,

a_0 and a_2 refer to the 3D s-wave scattering lengths of the atoms in the scattering channels with total spin $F=0$ and $F=2$, respectively. In contrast, the spin-dependent nonlinear term $c_2\mathbf{F}\cdot\mathbf{f}$ accounting for interactions among the hyperfine levels contains the coupling constant $c_2=4\pi\hbar^2(a_2-a_0)/(3M)$ and spin density $\mathbf{F}=(F_x,F_y,F_z)$, whose $j=\{x,y,z\}$ component is $F_j=\Psi^\dagger_{m_z}f_j\Psi_{m_z}$ where f_j denote the spin-1 matrices. As discussed in the main text, we focus on the ^{7}Li condensate possessing strong ferromagnetic interactions, that is $c_2<0$. The 3D external harmonic confinement $V_{\rm trap}=\frac{1}{2}M(\omega_x^2x^2+\omega_y^2y^2+\omega_z^2z^2)$ is characterized by the in-plane trap frequency $\omega_x\approx\omega_y$ and the out-of-plane one ω_z. These obey the condition $\omega_z\gg\omega_x\approx\omega_y$, which restricts the atomic motion in 2D. Throughout, we consider the experimentally used trap frequencies $(\omega_x,\omega_y,\omega_z)=2\pi\times(7,8,635)$ Hz. Moreover, the length and energy scales of the system are expressed in terms of the harmonic oscillator length $l_{\rm osc}=\sqrt{\hbar/M\omega_x}$ and the energy quanta $\hbar\omega$. For convenience of our simulations, we further cast the 3D Gross–Pitaevskii equation (2) into a dimensionless form by rescaling the spatial coordinates as $x'=x/l_{\rm osc}$, $y'=y/l_{\rm osc}$ and $z'=z/l_{\rm osc}$, the time as $t'=\omega_x t$ and the wavefunction as $\Psi_{m_z}(x',y',z')=\sqrt{(l_{\rm osc}^3/N)}\Psi_{m_z}(x,y,z)$. See, for example, refs. 59,60 for further details.

Depending on the relative strength of $q/(|c_2|n)$, it is possible to realize a rich phase diagram containing first- and second-order phase transitions as described in ref. 37. For instance, the quantum critical point $q=q_{\rm c}=2|c_2|n_{\rm peak}$, with $n_{\rm peak}$ being the condensate peak density around the trap centre, separates the so-called unmagnetized polar state in which all atoms are in the $m_z=0$ state from the easy-plane ferromagnetic phase with all m_z states being occupied. The latter phase occurs within the interval $0<q<q_{\rm c}$ and is characterized by the order parameter $\mathbf{F}_\perp=F_x+\mathrm{i}F_y$ for the transverse magnetization[25], where $F_x=[\Psi_1^*\Psi_0+\Psi_0^*(\Psi_1+\Psi_{-1})+\Psi_{-1}^*\Psi_0]/(\sqrt{2}n)$ and $F_y=\mathrm{i}[-\Psi_1^*\Psi_0+\Psi_0^*(\Psi_1-\Psi_{-1})+\Psi_{-1}^*\Psi_0]/(\sqrt{2}n)$. On the other hand, for $q<0$, the ground state corresponds to an easy-axis ferromagnetic phase where the magnetization lies along the z axis and the relevant order parameter is the longitudinal magnetization $F_z=|\Psi_{+1}|^2-|\Psi_{-1}|^2/n$.

Initial state preparation using quantum and thermal fluctuations

The initial state of the spin-1 gas (the easy-axis polar state) was realized at $q=2q_{\rm c}$, with the critical quadratic Zeeman shift $q_{\rm c}=2|c_2|n_{\rm peak}/h$. It is represented by the wavefunction

$$\Psi_{\rm polar}=(0,\Psi_0,0)^{\rm T}. \tag{3}$$

The latter was determined by numerically solving equation (2) using the split-time Crank–Nicholson method in imaginary time[61,62]. To trigger the dynamics, we performed a sudden change of the quadratic Zeeman coefficient q from its initial value $q_i/h=510$ Hz (polar state) to a final value $q_{\rm EA}/h=-200$ Hz (easy-axis state) or $q_{\rm Iso}/h=0$ (isotropic point).

To monitor the system's non-equilibrium dynamics, it was essential to consider the presence of quantum and thermal fluctuations on top of the initial zero-temperature mean-field state (equation (3)). This contribution seeded the ensuing dynamical instabilities occurring once q was quenched. We incorporated the impact of quantum and thermal effects exploiting the truncated Wigner approximation[39]. Namely, we expressed the wavefunction as $\Psi_I=\Psi_{\rm polar}+\boldsymbol{\delta}$, where $\boldsymbol{\delta}=(\delta^{+1},\delta^0,\delta^{-1})^{\rm T}$ is a noise vector constructed using the Bogoliubov quasi-particle modes of the system. Specifically, first, we calculated the steady-state solution ($\Psi_{\rm polar}$), which was subsequently perturbed according to the following ansatz $\Psi_{m_z}=\Psi_{\rm polar}+\epsilon\left(U_{m_z}\mathrm{e}^{\mathrm{i}\Omega t}+V^*_{m_z}\mathrm{e}^{-\mathrm{i}\Omega^* t}\right)$. Inserting this ansatz into equation (2) and linearizing with respect to the small amplitude ϵ leads to the corresponding energy eigenvalue problem, which was numerically solved through diagonalization, thus allowing us to determine the underlying eigenfrequencies $\{\Omega^j\}$ and eigenfunctions $\{U^j_{m_z},V^j_{m_z}\}$. For the polar steady state, where $\Psi_{\pm1}=0$ and $\Psi_0=\Psi_0$, the respective eigenvalue problem reads

$$\begin{pmatrix}U_0\\V_0\\U_1\\V_1\\U_{-1}\\V_{-1}\end{pmatrix}\begin{pmatrix}a&b&0&0&0&0\\-b^*&-a&0&0&0&0\\0&0&c&0&0&d\\0&0&0&-c&-d^*&0\\0&0&0&d&c&0\\0&0&-d^*&0&0&-c\end{pmatrix}=\Omega\begin{pmatrix}U_0\\V_0\\U_1\\V_1\\U_{-1}\\V_{-1}\end{pmatrix}. \tag{4}$$

Here, the matrix elements are given by $a=-\frac{1}{2}\nabla_\perp^2+V-\mu+2c_0|\Psi_0|^2$, $b=c_0(\Psi_0)^2$, $c=-\frac{1}{2}\nabla_\perp^2+V_{\rm trap}-\mu+q$ and $d=c_2(\Psi_0)^2$ with μ being the system's chemical potential. Having at hand the eigenmodes $\{U^j_{m_z},V^j_{m_z}\}$ and eigenvalues Ω^j, it is possible to express the noise field in the form $\delta_{m_z}=\sum_{j>0}U^j_{m_z}\beta^j_{m_z}+(V^j_{m_z})^*(\beta^j_{m_z})^*$. That is, we decompose it in terms of the low-lying collective modes of the initial state, which are weighted by the random-valued coefficients $\beta^j_{m_z}$. These coefficients are generated as

$$\beta^j_{m_z=\pm1}=\frac{x_j+\mathrm{i}y_j}{2}\quad\text{and}\quad\beta^j_{m_z=0}=\sqrt{\left(\bar{n}_j+\frac{1}{2}\right)}\frac{x_j+\mathrm{i}y_j}{\sqrt{2}}, \tag{5}$$

where x_j and y_j are random values taken from a normally distributed Gaussian distribution characterized by zero mean and unit variance, and $\bar{n}_j=(\mathrm{e}^{\Omega^j\hbar/(K_{\rm B}T)}-1)^{-1}$ denotes the mean thermal occupation of the Bose–Einstein condensate at temperature T. Notice also that the constant 1/2 factor in equation (5) stems from the vacuum noise. In this sense, the initial state of the system comprises a condensate with thermal excitations for the $m_z=0$ and only vacuum noise for the $m_z=\pm1$ components. In the experiment, the initial thermal fraction detected was less than 5%. To take this into account within our simulations, we used $T=35$ nK as the system temperature, for which the average thermal fraction was approximately 4% of the total atom number. Note that the number of thermal atoms is $N_{\rm T}=\int\mathrm{d}\boldsymbol{r}\left[\sum_j\{[(U^j_{m_z=0})^2+(V^j_{m_z=0})^2]\bar{n}_j+(V^j_{m_z=0})^2\}\right]$, see also ref. 39 for the relation between the thermal fraction and the temperature of the condensate. Note that we also explored with our simulations the effect of varying the initial temperatures while ensuring that the thermal fraction remained below 6%, as per the experimental conditions. Interestingly, we found that such temperature variations had no discernible impact on the coarsening dynamics. Finally, in order to render the observables of interest independent of the presence of the above-discussed noise factors, we employ multiple realizations, for example, for a specific quench, and afterwards perform an averaging. Typical samples leading to a converged behaviour of the observables of interest consist of 500 different realizations.

Data availability

Source data are provided with this paper.

References

54. Hild, S. et al. Far-from-equilibrium spin transport in Heisenberg quantum magnets. *Phys. Rev. Lett.* **113**, 147205 (2014).
55. Neely, T. W., Samson, E. C., Bradley, A. S., Davis, M. J. & Anderson, B. P. Observation of vortex dipoles in an oblate Bose–Einstein condensate. *Phys. Rev. Lett.* **104**, 160401 (2010).
56. Kwon, W. J., Moon, G., Seo, S. W. & Shin, Y. Critical velocity for vortex shedding in a Bose–Einstein condensate. *Phys. Rev. A* **91**, 053615 (2015).
57. Choi, J.-y., Kwon, W. J. & Shin, Y.-i. Observation of topologically stable 2D skyrmions in an antiferromagnetic spinor Bose–Einstein condensate. *Phys. Rev. Lett.* **108**, 035301 (2012).
58. Inouye, S. et al. Observation of vortex phase singularities in Bose–Einstein condensates. *Phys. Rev. Lett.* **87**, 080402 (2001).

59. Mukherjee, K., Mistakidis, S. I., Kevrekidis, P. G. & Schmelcher, P. Quench induced vortex-bright-soliton formation in binary Bose–Einstein condensates. *J. Phys. B: At. Mol. Opt. Phys.* **53**, 055302 (2020).
60. Kwon, K. et al. Spontaneous formation of star-shaped surface patterns in a driven Bose–Einstein condensate. *Phys. Rev. Lett.* **127**, 113001 (2021).
61. Crank, J. & Nicolson, P. A practical method for numerical evaluation of solutions of partial differential equations of the heat-conduction type. *Math. Proc. Camb. Philos. Soc.* **43**, 50–67 (1947).
62. Antoine, X., Bao, W. & Besse, C. Computational methods for the dynamics of the nonlinear Schrödinger/Gross–Pitaevskii equations. *Comput. Phys. Commun.* **184**, 2621–2633 (2013).

Acknowledgements

We acknowledge discussions with I. Bloch, S.-B. Chung, F. Fang, T. Hilker, G. C. Katsimiga, P. G. Kevrekidis, K. Kim, S. K. Kim, S. Majumder, S. M. Reimann and Y. Shin. K.M. acknowledges the PARAM Shakti at the Indian Institute of Technology Kharagpur, a national supercomputing mission, Government of India, for providing computational resources. J.-y.C. is supported by the Samsung Science and Technology Foundation (Grant No. BA1702-06), a National Research Foundation of Korea (NRF) grant (Project Nos. RS-2023-00207974 and 2023M3K5A1094812) and the KAIST UP programme. S.I.M. and H.R.S. acknowledge support from the NSF through a grant to the Institute for Theoretical Atomic Molecular and Optical Physics at Harvard University. K.M. is financially supported by the Knut and Alice Wallenberg Foundation (Grant No. 2018.0217) and the Swedish Research Council and also acknowledges the Ministry of Human Resource Development, Government of India, for a research fellowship at the early stages of this work.

Author contributions

All authors contributed substantially to the work presented in this manuscript. S.-J.H., K.K., J.S. and J.H. maintained the experimental apparatus and collected the data. S.-J.H., K.K. and J.S. analysed the data. K.M. and S.M. performed the numerical simulations. This work was supervised by S.I.M., H.R.S. and J.-y.C.

Competing interests

The authors declare no competing interests.

Additional information

Extended data Extended data are available for this paper at https://doi.org/10.1038/s41567-023-02339-2.

Supplementary information The online version contains supplementary material available at https://doi.org/10.1038/s41567-023-02339-2.

Correspondence and requests for materials should be addressed to Jae-yoon Choi.

Peer review information *Nature Physics* thanks the anonymous reviewers for their contribution to the peer review of this work.

https://doi.org/10.1038/s41567-023-02339-2

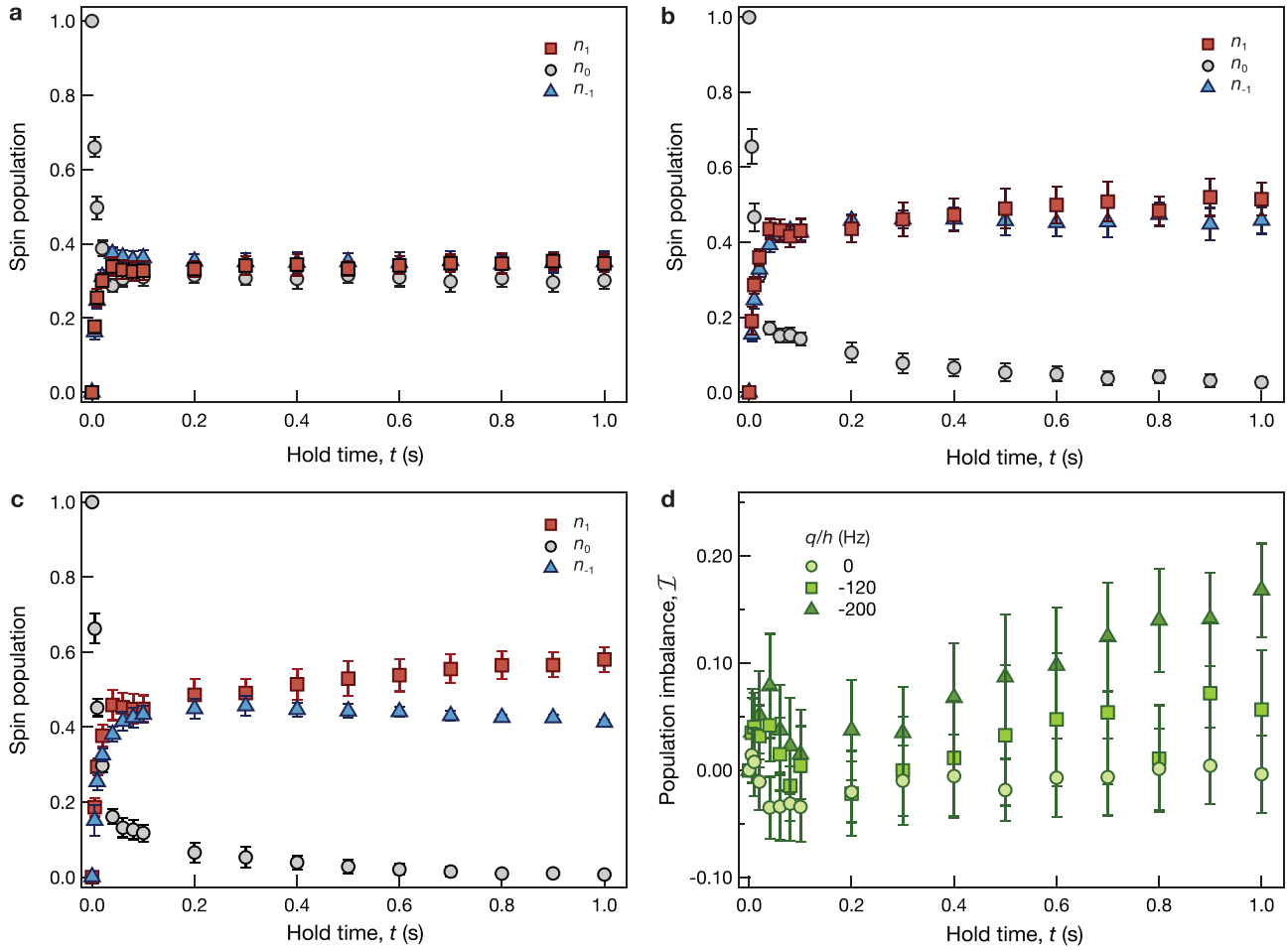

Extended Data Fig. 1 | Spin populations after quenching the quadratic Zeeman energy. a, After quenching to the isotropic ferromagnetic phase ($q/h = 0$ Hz), the atoms in the spin $|0\rangle$ state rapidly decay and create spin $|\pm1\rangle$ states. The spin population reach a steady state after 100 ms with equal population $(n_1, n_0, n_{-1}) \simeq (1/3, 1/3, 1/3)$. During the whole coarsening dynamics, the spin population for all spin states remains constant. In the easy-axis ferromagnetic phase (**b**,$q/h = -120$ Hz and **c**,$q/h = -200$ Hz), the initial $|0\rangle$ state rapidly disappear and generate equal population of the spin $|\pm1\rangle$ state. The residual spin component in the $|0\rangle$ state during the coarsening dynamics is attributed to the spin vector along the horizontal plane at the domain wall (Extended Data Fig. 4). Because of the microwave dressing field, the spin population gradually changes. **d**, Time evolution of spin population imbalance ($\mathcal{I} = n_1 - n_{-1}$) under different quadratic Zeeman energy. The population imbalance is noticeable in the deep easy-axis regime ($q/h = -200$ Hz), but its impact on the domain length is not significant as shown in Fig. 2. Each data point is obtained with more than 100 independent experimental runs, and the error bars represent one standard error of the mean.

https://doi.org/10.1038/s41567-023-02339-2

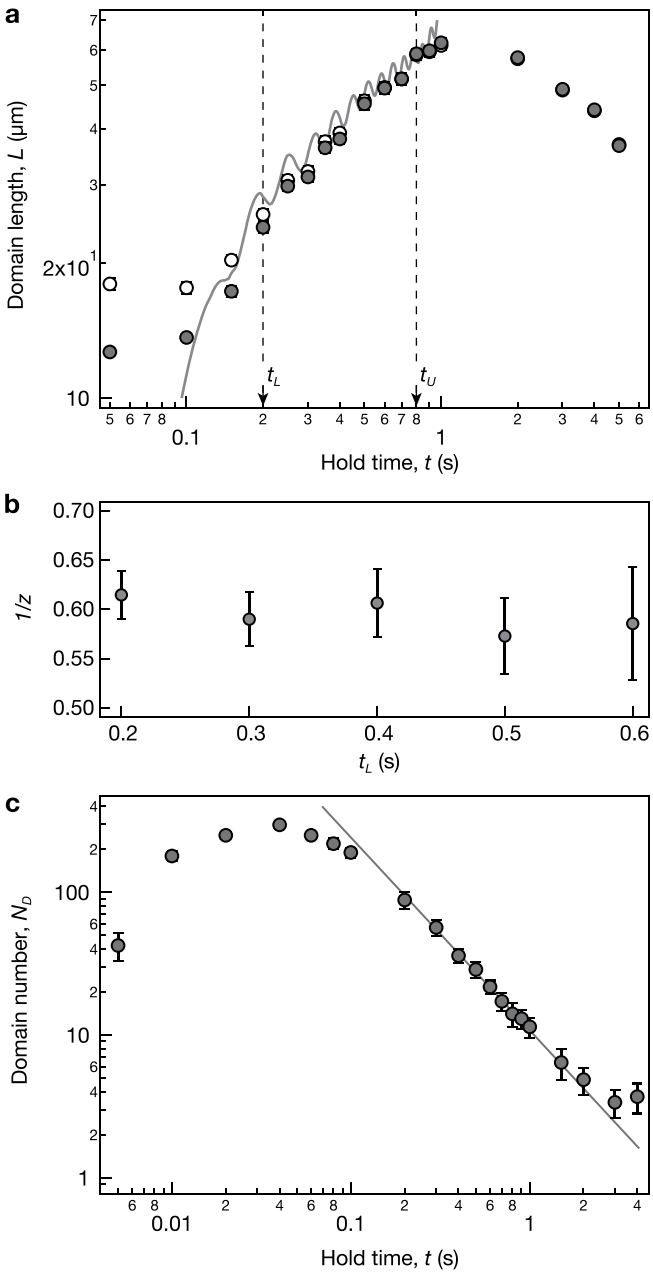

Extended Data Fig. 2 | Full-time evolution of coarsening dynamics and scaling exponents in the easy-axis ferromagnetic phase. a, Domain length $L(t)$ in the full time evolution accessible during the experiment. Closed (open) circles represent the domain length after (without) deconvolution. Dashed lines represent the scaling time interval $t \in [0.2\,\mathrm{s}, 0.8\,\mathrm{s}]$. The lower bound for the time interval is chosen to ensure that the condensate enters into the coarsening stage after the quench.The upper bound of the time interval is limited by the finite size of the system and lifetime lifetime of the condensate. **b**, Dependence of the scaling exponents $1/z$ on the lower bound for the time interval t_L. The error bars indicate the 1σ confidence interval of the fit parameters. **c**, Number of magnetic domains after the quench. The domain number N_D is counted by using the Hoshen-Koppelman algorithm (details are available in Supplementary Information). The domain number follows the power law decay (solid line), $N_D \sim t^{-2/z}$ with $1/z = 0.63(4)$.

https://doi.org/10.1038/s41567-023-02339-2

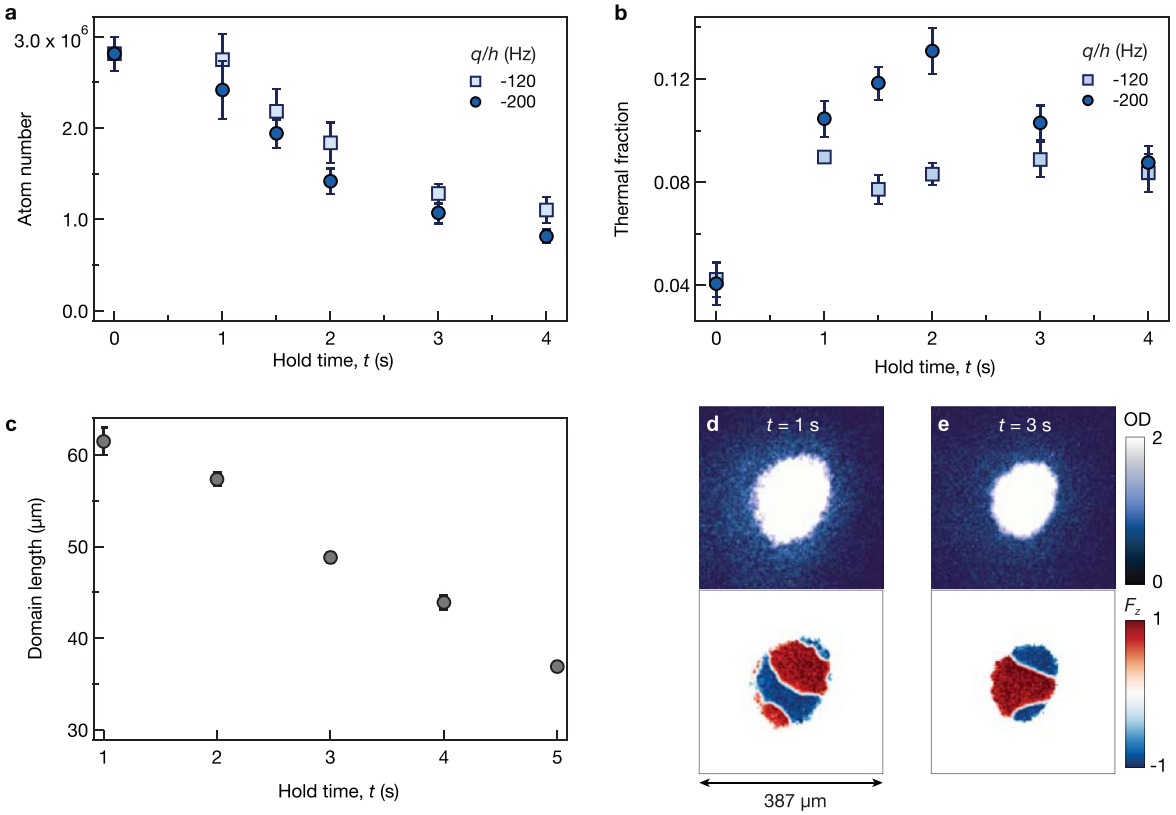

Extended Data Fig. 3 | Effect of the microwave dressing on the spinor Bose gas. a, Long-time evolution of the atom number and **b**, thermal fraction at $q/h = -120$ Hz (square, light blue) and -200 Hz (circle, dark blue). **c**, Long-time evolution of the domain length in the easy axis quench $q/h = -200$ Hz. After the coarsening terminated ($t = 1$ s), the domain length is decreased from 61 μm to 57 μm with additional 1 s of hold time. It implies that the domain length during the universal dynamics $t \in [0.2\,\text{s}, 0.8\,\text{s}]$ could be underestimated by 5%. **d,e** Absorption images (top) and the magnetization density (bottom) at different hold times (see legends). Domain size is reduced as a result of the atom loss. Each data point is obtained with 40 different experimental realisation, and the error bars denote one standard error of the mean.

https://doi.org/10.1038/s41567-023-02339-2

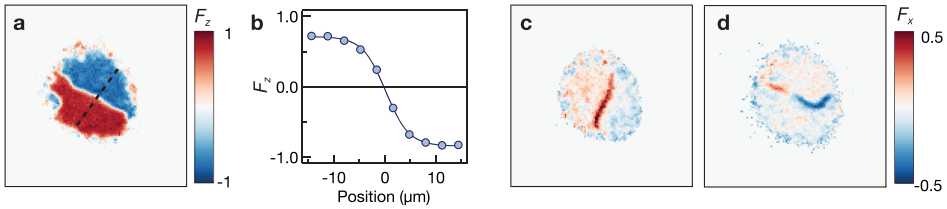

Extended Data Fig. 4 | Magnetic domain wall in the easy-axis ferromagnetic phase. a, Magnetization F_z after 1.5 s of hold time, and **b**, the cross-section profile across the magnetic domain. The solid line is a fit curve $F_z(r) = F_{z0}\tanh(r/\xi_d)$ with $\xi_d = 4.5(2)$ μm. **c,d**, Magnetization along the horizontal axis F_x. The spin vectors could be aligned on the same axis (c, Bloch or Neel-type domain wall) or point in opposite directions (d, Bloch line). A long wavelength modulation of the horizontal spin vector could imply the presence of spin wave excitations in the magnetic domain.

https://doi.org/10.1038/s41567-023-02339-2

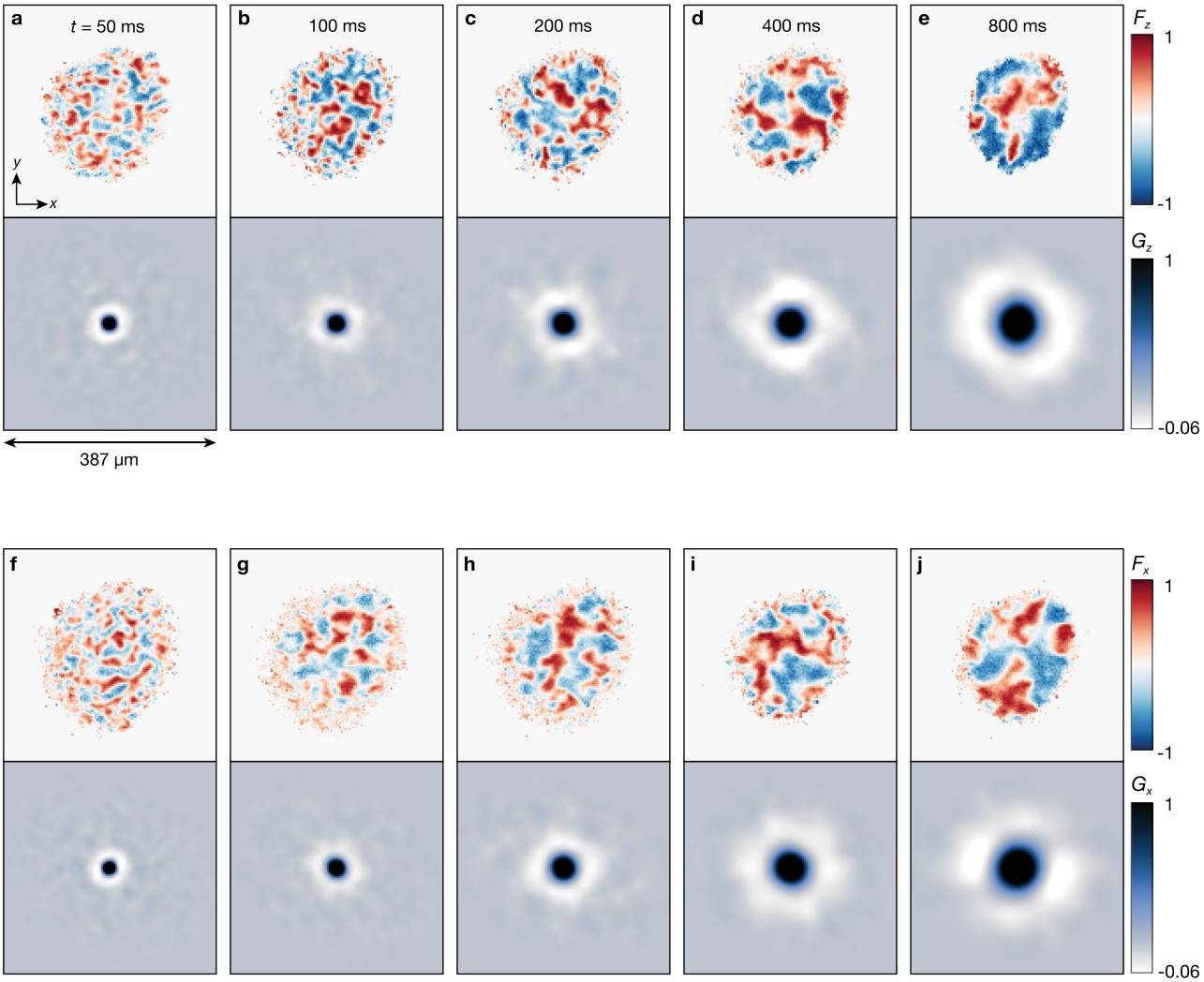

Extended Data Fig. 5 | Time evolution of spin domains in the isotropic ferromagnetic phase. a-e, Longitudinal magnetization F_z (upper) and its two-dimensional spin correlation functions $G_z(x, y)$ (below) at various hold times. **f-j**, Snapshots of transverse magnetization F_x, and the correlation functions $G_x(x, y)$. In contrast to the easy-axis phase, in the spin isotropic point, coarsening dynamics are observed in both axes, and the domain boundaries are much broader than those of the $q < 0$ spin domains. The spin correlation functions are averaged over 100 different realizations at a given hold time.

https://doi.org/10.1038/s41567-023-02339-2

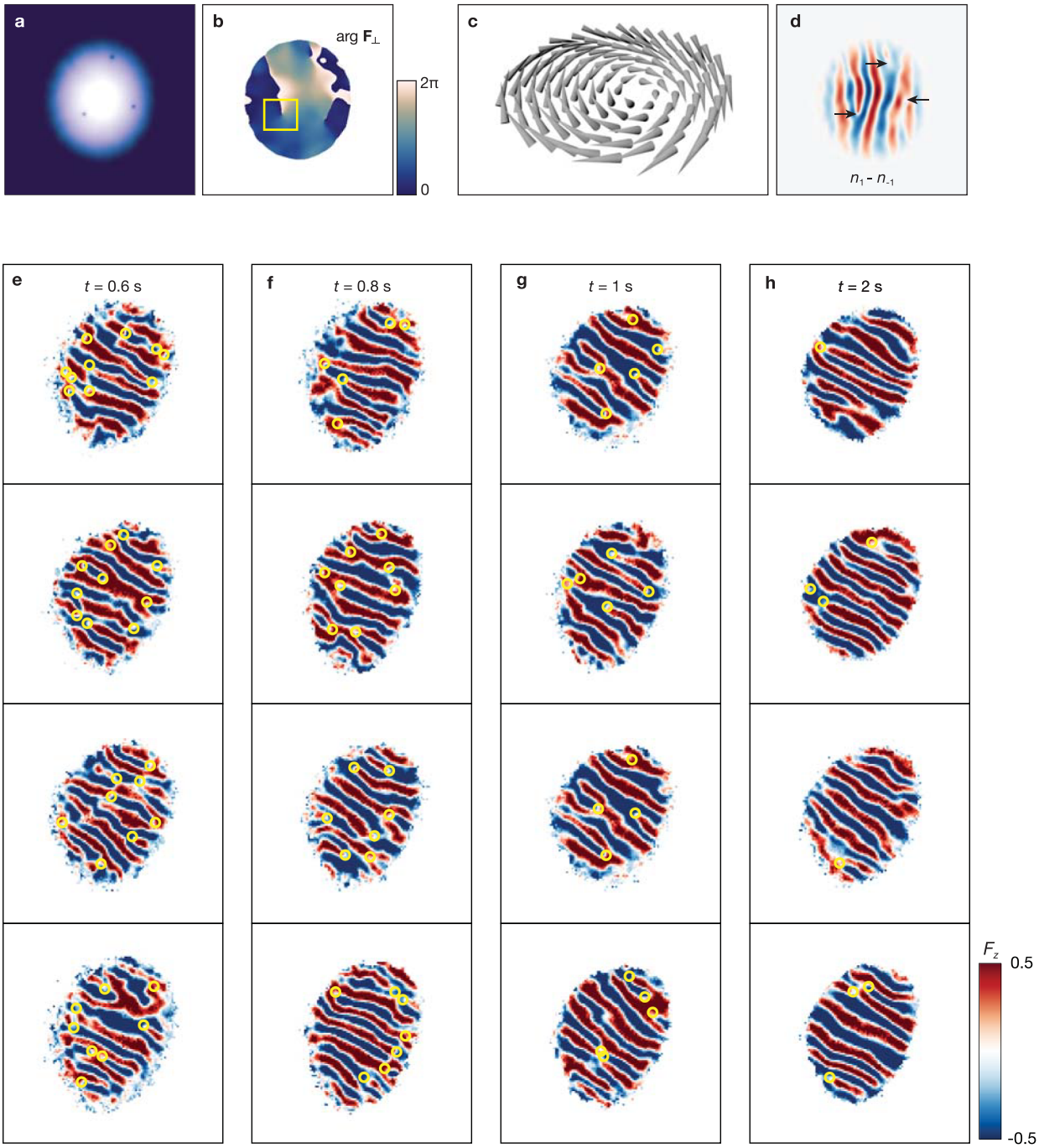

Extended Data Fig. 6 | Numeric simulations of the matter-wave interference for the $\mathbb{Z}_2$ spin vortices. a, Density profile and **b**, the argument of the transverse spin vector $\phi = \tan^{-1}(F_y/F_x)$ in the x-y plane after $t = 3.5$ s of domain coarsening dynamics at the spin isotropic point. The spin vortex can be identified from a phase jump around the vortex core (yellow box). **c**, Three dimensional spin vectors $\mathbf{F} = (F_x, F_y, F_z)$ in the x-y plane near the highlighted region (yellow box). Not only the in-plane spin vector but also the longitudinal spin vector turns around the vortex core, indicating the $\mathbb{Z}_2$ spin vortex. **d**, Simulated images after the matter-wave interference. The positions of the spin vortices are well-identified from fork-shaped patterns in the spin imbalance image. **e**–**h**, Representative experimental images after the matter-wave interference under various hold times (see distinct rows). All images are obtained by independent experimental runs. In the vortex-free region, the magnetization displays a connected stripe pattern, while the spin vortex shows a dislocation of the stripes to form the two-to-one fork-shaped patterns. The vortex positions are highlighted by yellow circles.